

Section 3

Computational studies including new techniques, parallel processing, GPUs.
Effects of model resolution.

Three-dimensional visualization of atmospheric fronts

A.S.Bezubtsev (Lyceum "Second school"), Ph.L.Bykov (Hydrometeorological Center of Russia), V.A.Gordin (National Research University - Higher School of Economics, Hydrometeorological Center of Russia)

We construct atmospheric fronts (AF) – thin surfaces separating generally homogeneous SYNOPTIC air masses using a set of meteorological fields: geopotential, temperature and wind. It can be useful for synoptic 3D analysis of the Earth atmosphere. The analysis can be organized on-line, e.g. during an aircraft's flight.

Firstly we construct lines of atmospheric fronts (AF) at isobaric ($p=\text{const}$) levels, see [1, 3]. In order to do this, we use differential geometry invariants, such as the Gaussian principal curvature of isotherms and the vector analogue of this invariant for horizontal wind. Basing on the initial meteorological fields (geopotential, temperature and wind), we firstly evaluate independent predictors, and then their linear combination – the field of the final predictor. The weights in this combination are being matched through numerical optimization. The corresponding quality criterion is the maximum difference between temperature correlation function for pairs of geographical points separated by AF and pairs lying at a given isobaric level in common synoptic mass.

At the second step, we connect closely lying lines at adjacent isobaric levels and construct 3D AF surfaces, see Figure 1. These surfaces have a complex geometric and topological structure and change quickly over time.

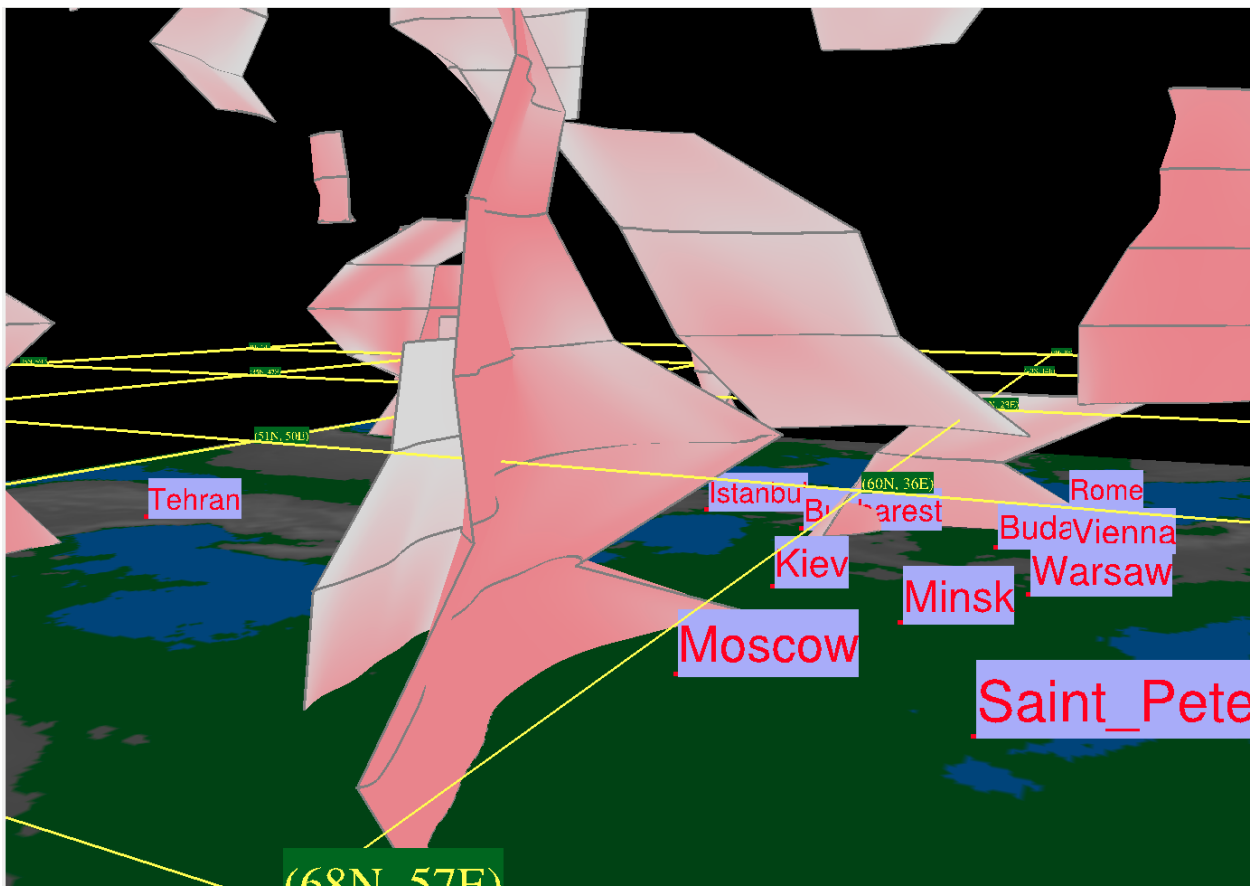


Figure 1. View of the field of fronts over the European region. Date & Time: 6 March 2019, 12:00 GMT.

Visualization of the AF surface improves understanding of the specific SYNOPTIC situation and accelerates understanding of the meteorological situation during an aircraft's flight. The AF geometry can influence precipitation [4].

Methodology

The AF curves obtained as the output of the algorithm described in [1, 3] are presented not in analytical form, but as some sets of points.

We approximate the curves using the Bezier approximation [5] and represent them as sets of $N=200$ points uniformly distributed along the length of the curve.

We have developed a measure of the "affinity" for a pair of curves, located at adjacent isobaric levels, reflecting the intuitive geometric continuity.

Acknowledgements

The article was prepared within the framework of the Academic Fund Program at the National Research University Higher School of Economics (HSE) in 2018 – 2019 (grant No. 18-05-0011) and by the Russian Academic Excellence Project «5-100».

Literature

1. Ph.L.Bykov, V.A.Gordin. Objective Analysis of the Structure of Three-Dimensional Atmospheric Fronts. *Izvestiya, Atmospheric and Oceanic Physics*, 48(2), 2012, PP. 152-168. SpringerLink: <https://link.springer.com/article/10.1134%2FS0001433812020053>
2. V.A.Gordin. *Mathematics, Computer, Weather Forecasting, and Other Scenarios of Mathematical Physics*, 733pp., Moscow, Fizmatlit, 2010, 2013 (In Russian).
3. O.A.Alduchov, Ph.L.Bykov, V.A.Gordin. Large-Scale Three-Dimensional Correlation Functions for the Earth's Atmosphere. "Yaroslavl pedagogical Bulletin, Series of Natural Sciences", №4 (2011) PP.36-43. (In Russian).
4. Ph.L.Bykov, V.A.Gordin. On Statistical Connection between Atmospheric Fronts and Precipitation. *Proceedings of the Hydrometeorological Research Center of the Russian Federation*. 2012, issue 348, PP.184—194 (In Russian).
5. M.K.Agoston. *Computer Graphics and Geometric Modelling: Implementation and Algorithms*, 2005. PP.396 – 404 SpringerLink: <https://link.springer.com/book/10.1007/b138805>

Laplace Transforms and Exponential Integrators

Peter Lynch

School of Mathematics & Statistics, UCD, Ireland

The accuracy and efficiency of weather and climate models has been greatly enhanced by the introduction of better numerical algorithms for the solution of the equations of motion. Two of the most notable schemes are the semi-implicit (SI) scheme for treating the gravity-wave terms and the semi-Lagrangian scheme for advection processes.

Many operational NWP models use a semi-implicit scheme for time integration, increasing efficiency by enabling the use of a large time step. But this comes at a price: stabilization is achieved by slowing down the high-frequency gravity waves. However, the meteorologically significant components of the flow are also distorted by the time averaging of the SI scheme.

It was pointed out in Lynch & Clancy (2016) that the LT method with analytic inversion gives an exact treatment of the linear modes. This is due to the fact that the LT scheme does not involve time-averaging of the linear terms. Harney & Lynch (2019) describe a Laplace transform integration scheme in a baroclinic model and show that it yields more accurate forecasts than SI. A version of the LT scheme for use with semi-Lagrangian advection is under development.

An alternative way of achieving accuracy is to use an exponential integrator (e.g., Pudykiewicz and Clancy, 2019; Peixoto and Schreiber, 2019). In this note we demonstrate the close relationship between Laplace transform integration and exponential integrators.

LTI and Exponential Integrators

We may write the model equations in the form

$$\frac{\partial \mathbf{X}}{\partial t} = \mathbf{L}\mathbf{X} + \mathbf{N}(\mathbf{X}). \quad (1)$$

Assuming that the matrix \mathbf{L} has an orthogonal eigenvector matrix \mathbf{E} with $\mathbf{L}\mathbf{E} = \mathbf{E}\mathbf{\Lambda}$, we have

$$\begin{aligned} \mathbf{L} &= \mathbf{E}\mathbf{\Lambda}\mathbf{E}^T, & \mathbf{\Lambda} &= \mathbf{E}^T\mathbf{L}\mathbf{E} & \text{and} & & e^{\mathbf{L}t} &= \mathbf{E}e^{\mathbf{\Lambda}t}\mathbf{E}^T \\ \mathbf{L}^{-1} &= \mathbf{E}\mathbf{\Lambda}^{-1}\mathbf{E}^T, & \mathbf{\Lambda}^{-1} &= \mathbf{E}^T\mathbf{L}^{-1}\mathbf{E} & \text{and} & & e^{\mathbf{\Lambda}t} &= \mathbf{E}^T e^{\mathbf{L}t} \mathbf{E} \end{aligned}$$

If the solution of (1) at time $t_n = n\Delta t$ is known, the Laplace transform with this initial time is

$$s\widehat{\mathbf{X}} - \mathbf{X}^n = \mathbf{L}\widehat{\mathbf{X}} + \widehat{\mathbf{N}}$$

where $\mathcal{L}\{\mathbf{X}\} = \widehat{\mathbf{X}}$ is the Laplace transform of the state vector. Solving for this, we get

$$\widehat{\mathbf{X}} = (s\mathbf{I} - \mathbf{L})^{-1}[\mathbf{X}^n + \widehat{\mathbf{N}}]. \quad (2)$$

We note that

$$(s\mathbf{I} - \mathbf{L})^{-1} = \mathbf{E}(s\mathbf{I} - \mathbf{\Lambda})^{-1}\mathbf{E}^T$$

and also note the transforms

$$(s\mathbf{I} - \mathbf{\Lambda})^{-1} = \mathcal{L}\{\exp(\mathbf{\Lambda}t)\} \quad \text{and} \quad (s\mathbf{I} - \mathbf{L})^{-1} = \mathcal{L}\{\exp(\mathbf{L}t)\}.$$

We can write the nonlinear term as

$$(s\mathbf{I} - \mathbf{L})^{-1}\widehat{\mathbf{N}} = \mathcal{L}\{\exp(\mathbf{L}t)\} \cdot \mathcal{L}\{\mathbf{N}\}.$$

The convolution theorem allows this to be written

$$(s\mathbf{I} - \mathbf{L})^{-1}\widehat{\mathbf{N}} = \mathcal{L}\left\{\int_{t_n}^t \exp(\mathbf{L}(t-\tau))\mathbf{N}(\tau) d\tau\right\}.$$

The transformed equation (2) now becomes

$$\widehat{\mathbf{X}} = \mathcal{L}\{\exp(\mathbf{L}t)\}\mathbf{X}^n + \mathcal{L}\left\{\int_{t_n}^t \exp(\mathbf{L}(t-\tau))\mathbf{N}(\tau) d\tau\right\}$$

We invert this at time $t_{n+1} = t_n + \Delta t$ to get

$$\mathbf{X}^{n+1} = e^{\mathbf{L}t_{n+1}}\mathbf{X}^n + e^{\mathbf{L}t_{n+1}} \int_{t_n}^{t_{n+1}} e^{-\mathbf{L}\tau} \mathbf{N}(\tau) d\tau \quad (3)$$

We note that (3) is formally identical to Equation (8) of Peixoto and Schreiber (2019) which they call the variation-of-constants formula.

We have thus established a close relationship between the Laplace transform scheme and exponential integrators.

Approximating the Nonlinear Term

The convolution term must be evaluated by approximate means, since it involves unknown quantities. Suppose we evaluate the nonlinear term at time t_n and assume that it is constant throughout the timestep (t_n, t_{n+1}) . Then the convolution integral can be evaluated, giving

$$\begin{aligned} \mathbf{X}^{n+1} &= e^{\mathbf{L}t_{n+1}}\mathbf{X}^n + e^{\mathbf{L}t_{n+1}} \left(\int_{t_n}^{t_{n+1}} e^{-\mathbf{L}\tau} d\tau \right) \mathbf{N}^n \\ &= e^{\mathbf{L}t_{n+1}}\mathbf{X}^n + (-\mathbf{L})^{-1} [\mathbf{I} - \exp(\mathbf{L}\Delta t)] \mathbf{N}^n . \end{aligned}$$

Assuming a small time-step, this reduces to

$$\mathbf{X}^{n+1} = e^{\mathbf{L}t_{n+1}}\mathbf{X}^n + \Delta t \mathbf{N}^n .$$

This is perhaps the simplest version of an exponential integrator. There is a wide range of more sophisticated and accurate approximations of the convolution integral. For example, we might estimate N at the centre of the time step by extrapolation $N^{n+1/2} = (3N^n - N^{n-1})/2$. Many other possibilities exist.

The time-averaging of the SI scheme also results in an error in the nonlinear term, even when this term is constant (see Harney & Lynch, 2019, Eq. 3). In this ideal case, the LT scheme has no error in the nonlinear term (*loc. cit.*, Eq. 4).

References

- Harney, Eoghan & Peter Lynch, 2019: Laplace Transform Integration of a Baroclinic Model. *Quart. J. Roy. Met. Soc.*, **145**, 347–355.
- Lynch, Peter & Colm Clancy, 2016: Improving the Laplace Transform Integration Method. *Q. J. Roy. Met. Soc.*, **142**, 1196–1200
- Peixoto, Pedro da Silva & Martin Schreiber, 2019: Semi-Lagrangian Exponential Integration with application to the Rotating Shallow Water Equations. arXiv:1904.09189.
- Pudykiewicz, J & C Clancy, 2019: Integration of the Euler Equations with the Exponential Method. *Research Activities in Atmospheric and Oceanic Modelling* (2019 WGNE Blue Book), This Vol, pp. 3-07–3-08.

Integration of the Euler equations with the exponential method.

J. Pudykiewicz (1) & C. Clancy (2)

(1) RPN/A, ECCC, janusz.pudykiewicz@canada.ca

(2) Met Éireann, colm.clancy@met.ie

Most of the time integration schemes used in meteorological models are either semi-implicit or split-explicit. These choices are predetermined by a fundamental work of A. Robert and G. Marchuk from the late 1960s. The robustness and efficiency of both algorithms is undisputed, as proven by numerous examples of Numerical Weather Prediction (NWP) models [2]. In the last decade several attempts have been made to design the alternative methods of the time stepping (see the introductions in [1] and [2] for review). One of the emerging techniques is the exponential time integration, which is derived from the general principles of the theory of dynamic systems. The essence of the exponential method lies in the dynamic linearization of the meteorological equations combined with the analytical evaluation of a resolvent operator. The example of implementation of such a method in the icosahedral shallow water model is described in [1]. The main conclusion from this study is that the time step used can be increased six-fold with respect to the semi-implicit method, while still increasing accuracy of the model. The issue of efficiency of the exponential scheme was addressed in the separate study, which shows that the execution time may be comparable to the semi-implicit scheme, provided that some optimizations of the code are introduced [2] and [3]. The important question is whether or not the same results can be achieved for the compressible Euler equations. In our study, we use the equations for perturbations with respect to the height dependent reference state. In standard notation, the system under consideration can be written as follows

$$\begin{aligned}\partial_t \mathbf{v} &= -\mathbf{v} \nabla \mathbf{v} - c_p (\bar{\theta} + \theta') \nabla \pi' + g(\theta' / \bar{\theta}) \hat{\mathbf{z}} \\ \partial_t \pi' &= -\mathbf{v} \nabla \pi' - (R/c_v)(\bar{\pi} + \pi') \operatorname{div} \mathbf{v} + g(\mathbf{v} \cdot \hat{\mathbf{z}}) / c_p \bar{\theta} \\ \partial_t \theta' &= -\mathbf{v} \nabla \theta' - (\mathbf{v} \cdot \hat{\mathbf{z}}) \partial_z \bar{\theta}\end{aligned}$$

Fluid equations are discretized on a Cartesian grid using the fourth-order central finite difference approximation for space derivatives. Bottom no-flow through and cyclic lateral boundary conditions are imposed. The resulting set of semi-discrete Ordinary Differential Equations (ODEs) is solved with the exponential integration method with the analytic Jacobian as in [1]. The equations considered in this study are inviscid and the numerical noise is controlled with the help of the Shapiro filter.

We have selected two different initial conditions. In the first case, we consider two air bubbles with a small positive and negative buoyancy placed at different levels, while in the second case, a single bubble with negative buoyancy placed just below the upper lid. The first initial condition leads to a collision of the thermals, whereas the second one generates the gravity current splashing at the ground. The grid system used in the simulation of colliding thermals extends from the surface up to 5 km and has a horizontal length of 5 km, the corresponding sizes for the gravity current are 3 and 8 km respectively. The numerical mesh in both cases was homogeneous with a constant spacing of 20 m. All calculations in both cases were performed with the time step of 15 seconds giving the Courant number for acoustic waves around 250.

The results of the simulation of colliding thermals are depicted in Fig. 1. Evidently, the method is stable despite very long time steps and can capture a sharp contrast between the cold and warm bubbles. This observation is further reinforced by the results for the gravity current shown in Fig. 2, just at the time of impact and at a later stage when the flow changes direction from horizontal to vertical. The execution time for a single time step of the MATLAB code per grid point is about 0.00007 sec on a single 2.9 GHz Intel I9 core. The future work with the presented model will include testing of the other approximations of the space derivatives and the experiments with moist thermodynamics.

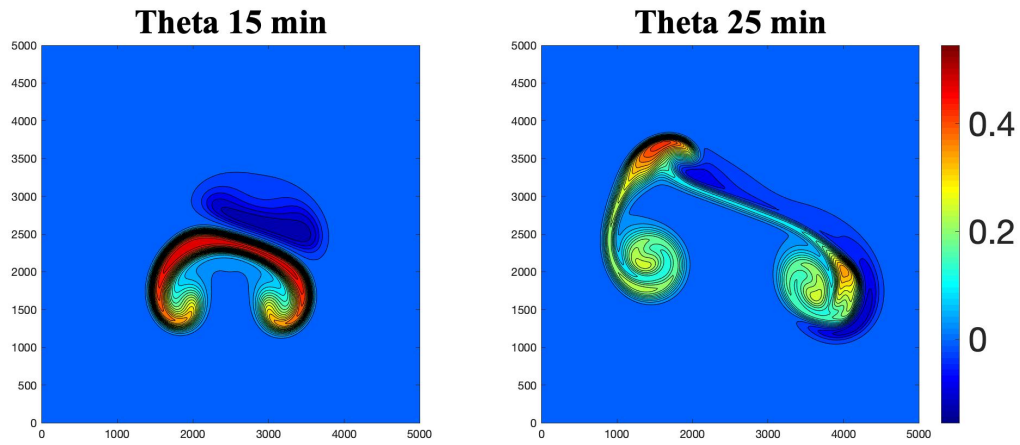


Fig. 1 Potential temperature perturbation in the convective element colliding with a negative buoyancy bubble.

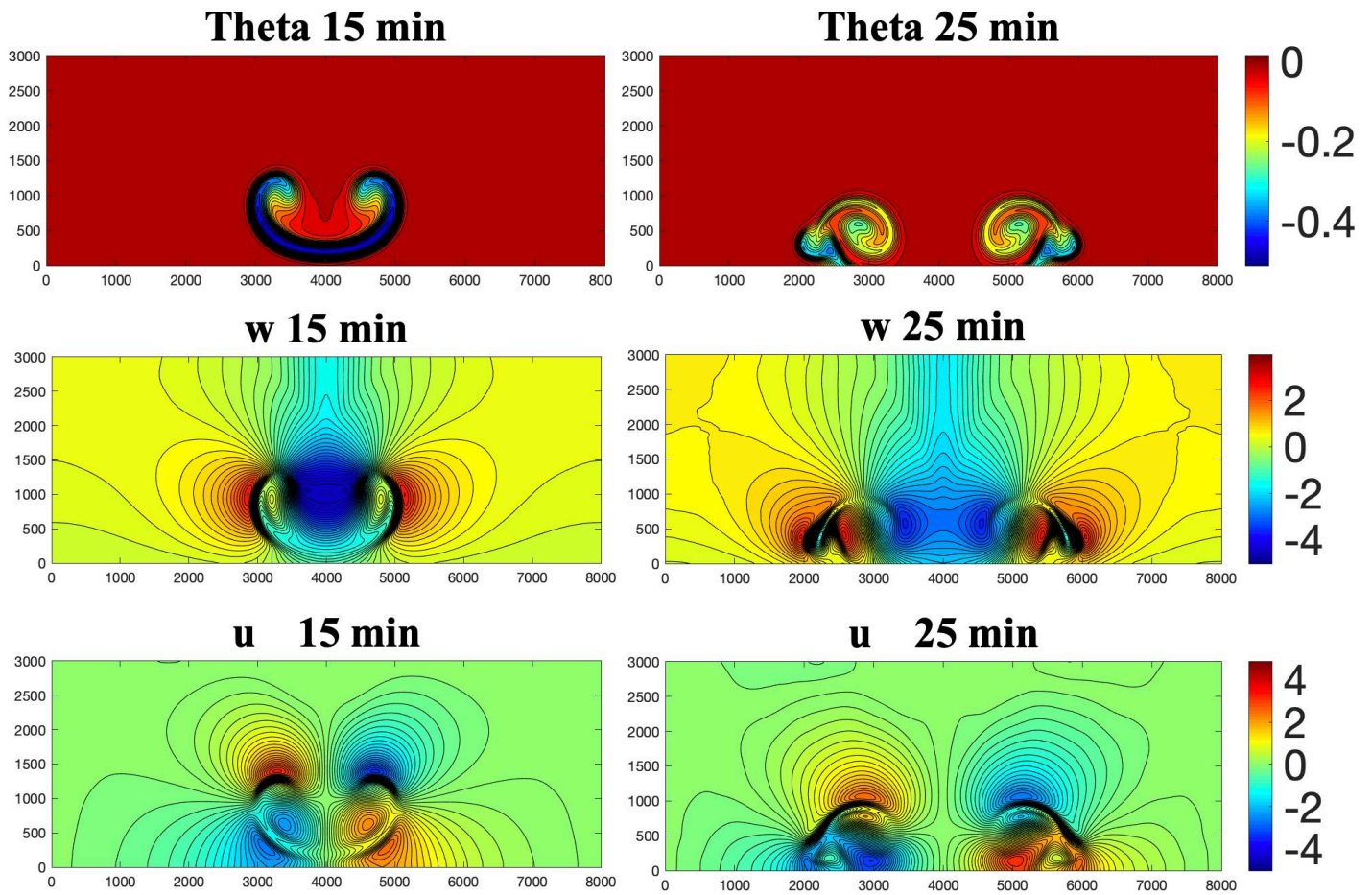


Fig. 2 Potential temperature perturbation and velocity components (m/s) in the descending cold bubble splashing on the surface.

References

- [1] Clancy C., J. Pudykiewicz (2013): On the use of exponential time integration methods in atmospheric models, *Tellus A*, 65.
- [2] Gaudreault S., J. Pudykiewicz (2016): An efficient time integration method for the numerical solution of the shallow water equations on the sphere, *J. Comp. Phys.*, 322, 827-848.
- [3] Vu Thai Luan, J. Pudykiewicz, D. R. Reynolds (2019): Further development of efficient and accurate time integration schemes for meteorological models, *J. Comp. Phys.*, 376, 317-337

Reasons for the cut-cell Eta skill vs. ECMWF in ensemble experiments ?

Katarina Veljovic ¹ and Fedor Mesinger ²

¹ Institute of Meteorology, University of Belgrade, Belgrade, Serbia (katarina@ff.bg.ac.rs)

² Serbian Academy of Sciences and Arts, Belgrade, Serbia (fedor.mesinger@gmail.com)

In Mesinger and Veljovic (2017, MV2017 later on) we have reported on an experiment in which the limited area cut-cell Eta model, driven by ECMWF (EC further on) 32-day ensemble members, achieved accuracy of large scales for an extended period clearly improved compared to that of its driver members. We have added to these results in our 2017 “Blue Book” contribution, and expanded on them yet some more in an extended conference preprint (Mesinger and Veljovic 2018, MV2018 later on).

With the ongoing developments of dynamical cores in numerous centers using a variety of approaches, we feel that still more attention to reasons for this cut-cell Eta skill is appropriate. One of the accuracy measures we used in MV2018 was the so called Extreme Dependency

Score (EDS). Some of its undesirable properties have been removed by the Symmetric Extreme Dependency Score (SEDS) and therefore in Fig. 1, left panel, we show number of “wins” in forecasting 250 hPa winds $> 45 \text{ m s}^{-1}$, according to SEDS scores, of the Eta (blue) vs. EC (red). Same, but for the Eta switched to use sigma (orange) is shown in the right panel.

For a synoptically specific information on the large scale skill of the three ensembles, in Fig. 2 contours are shown of winds of 45 m s^{-1} for each set of ensemble members, yellow-brown, along with the EC verification contours, red. It is seen that the Eta contours (middle), avoid some of the errors of the EC members (top), while with the Eta switched to sigma (bottom) some of the errors are reintroduced.

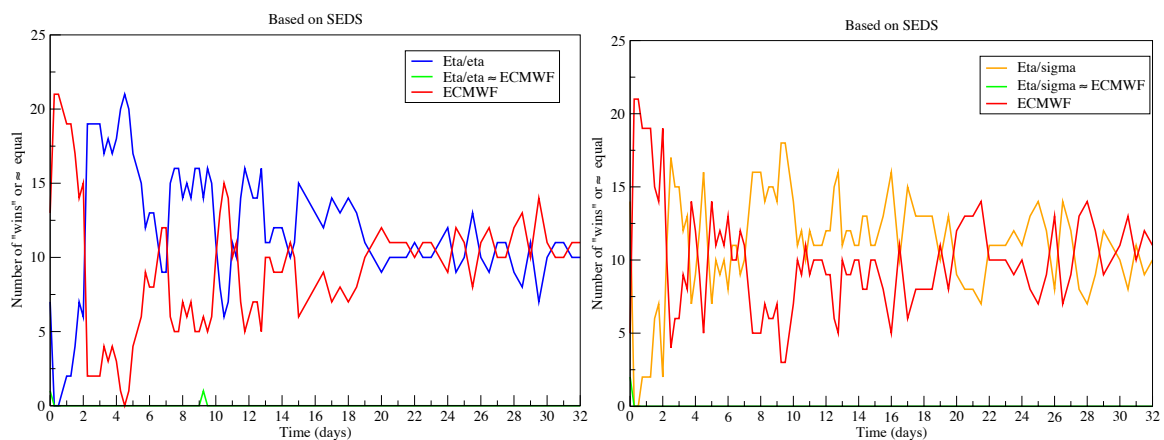


Fig. 1. Number of “wins” of one model vs. another, according to SEDS scores, in forecasting occurrence of 250 hPa winds $> 45 \text{ m s}^{-1}$; blue, Eta, red, their EC driver members. left panel. Same but for the Eta switched to use sigma, orange, right panel.

Since the resolution of the two Eta ensembles was until day 10 of the experiments about the same as that of the driver EC, the results shown strongly suggest that the Eta dynamical core includes features additional to the vertical coordinate responsible for the Eta skill vs. EC. Some of the possible candidates are discussed in MV2018.

References

Mesinger F, Veljovic K (2017) Eta vs. sigma: Review of past results, Gallus-Klemp test, and large-

scale wind skill in ensemble experiments. Meteorol. Atmos. Phys., **129**, 573-593. doi:10.1007/s00703-016-0496-3

Mesinger F, Veljovic K (2018) Cut-cell Eta: Some history, and lessons from its present skill. *Numerical Weather and Climate Modeling*, Serbian Academy of Sciences and Arts, 43-51. <https://www.sanu.ac.rs/wp-content/uploads/2018/09/NWCM-abstract.pdf#page=44>

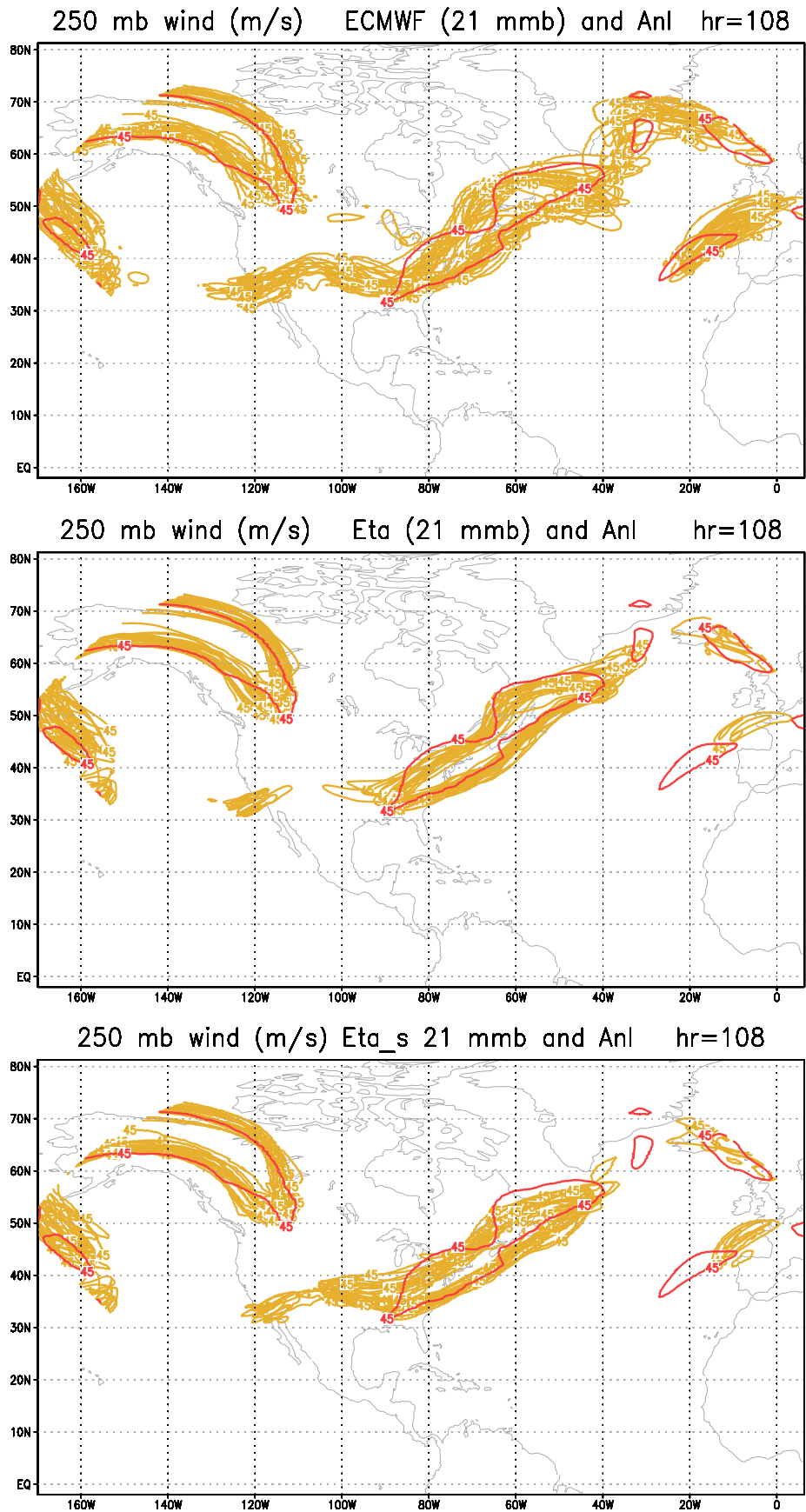


Fig. 2. Contours of the 250 hPa wind speeds of 45 m s⁻¹ of 21 members of the EC driver ensemble, upper panel, the Eta ensemble, middle panel, and the Eta/sigma ensemble, lower panel, all yellow-brown, and of the EC verification analysis, red; at 4.5 day lead time. (From MV2018).

Comparisons of high-resolution simulations of tropical cyclones with a single domain and nested domains

Weiguo Wang, Bin Liu, Zhan Zhang, Lin Zhu, Avichal Mehra* and Vijay Tallapragada*
IMSG@EMC/NCEP/NWS, *EMC/NCEP/NWS, College Park, MD 20740
Email: Weiguo.Wang@noaa.gov

1. Introduction

Currently global (regional) numerical weather prediction (NWP) models can be run in real time on a 10^4 (10^3)-meter scale at operational centers. However, such resolutions are still not high enough for simulations of tropical cyclones (TCs) which are characterized by multi-scale interactions on the order of 10^2 to 10^6 meters. Even with advances in computer technology, it is not yet practical to run NWP models with a very high resolution on all scales. To this end, the widely-used grid nesting technology will continue to play an important role. In the literature, there are reports regarding the impact of resolution and domain configurations on TC simulations. But there are few studies on direct comparisons of TC structures simulated over a single domain and nested domain. We designed an experiment using the Hurricane Weather and Research Forecast (HWRF) model to illustrate TC simulations using a triple nested domain configuration (TRIDOM) can be very close to those using a single domain configuration (ONEDOM) with the same resolution as the innermost nest domain, given proper feedback between domains. The former configuration uses significantly fewer resources and is hence more practical.

2. HWRF configurations

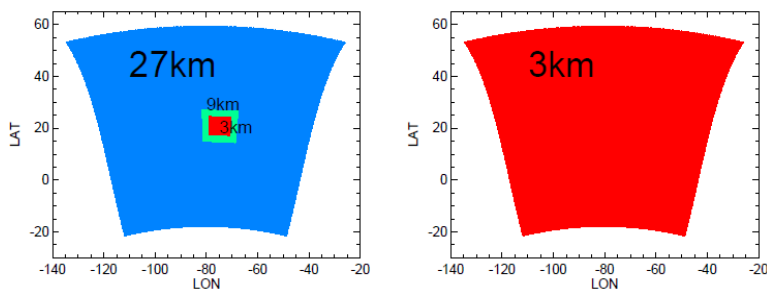


FIG. 1 Schematics of (left) 27-9-3km domains (TRIDOM) and (right) a single 3-km domain (ONEDOM).

In the TRIDOM simulations, HWRF was configured with three domains, a parent grid and two telescopic and movable 2-way nested grids that follow the storm. The parent domain covers approximately $80^\circ \times 80^\circ$ with 27-km grid spacing, and the two nested grids cover $12^\circ \times 12^\circ$ and $7^\circ \times 7^\circ$ with 9-km and 3-km horizontal grid spacing, respectively. The model top is 50hPa, with 61 levels in the vertical and approximately 18 levels

below 1000 m. Physics options include a GFDL surface layer coupled with a slab land surface model, Ferrier microphysics scheme, GFDL radiation schemes, simplified Arakawa-Schubert convective scheme (only for the parent and intermediate domains), and GFS PBL scheme. Lateral boundary conditions are derived from GFS forecasts. Initial conditions are derived from the GFS analysis and enhanced through a data assimilation system and vortex relocation technique. The configuration, boundary and initial conditions of the ONEDOM run are the same as TRIDOM, except that HWRF was run only over the TRIDOM parent domain with 3-km resolution (a full cloud resolving mode). In addition, in order to evaluate the impact of feedback between nest grids, TRIDOM was run using different values of feedback percentage.

3. Results and discussions

As a case study, the results of simulations of Hurricane Isaac (2012) initialized at 2012082518 are compared. For the TRIDOM simulations, HWRF with full two-way nesting (100% feedback) produced hurricane track and intensity forecasts which are better than those with one-way nesting (0% feedback) (Fig. 2). This implies the importance of multi-scale interactions of dynamic and physical

processes in hurricane simulations. Track forecasts from TRIDOM runs are closer to observations than from the ONEDOM run. Large-scale fields on the 27-km grid are closer to observations than those from the 3-km grid in the ONEDOM run. It is likely due to the performance of physics schemes with different resolutions, given that the use of a higher resolution should reduce the errors in numerical approximations. Many schemes were developed originally for simulations over coarse grids and may not work well for higher resolutions. The TRIDOM run with full feedback yields an intensity close to the ONEDOM run, suggesting that main TC features simulated in ONEDOM can be reproduced by the smaller nested domains in TRIDOM. Figure 3 shows that the size and depth of simulated TCs from the TRIDOM run with full 2-way feedback are very close to those from the run using a single large domain with 3-km resolution. So are the distributions of temperature perturbation and relative humidity (RH). The one-way feedback run of TRIDOM generated a deeper, smaller, and stronger TC than the single large domain.

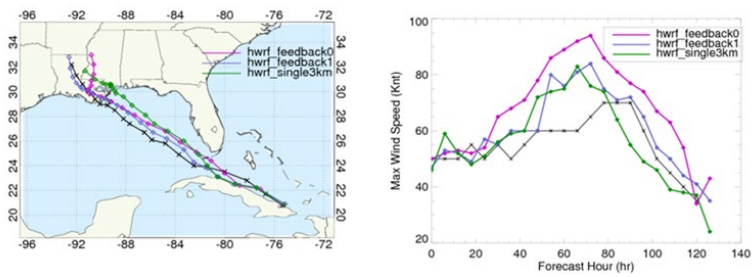


FIG. 2 Hurricane tracks and intensity. Black lines: best track data.

close to the ONEDOM run, suggesting that main TC features simulated in ONEDOM can be reproduced by the smaller nested domains in TRIDOM. Figure 3 shows that the size and depth of simulated TCs from the TRIDOM run with full 2-way feedback are very close to those from the run using a single large domain with 3-km resolution. So are the distributions of temperature perturbation and relative humidity (RH). The one-way feedback run of TRIDOM generated a deeper, smaller, and stronger TC than the single large domain.

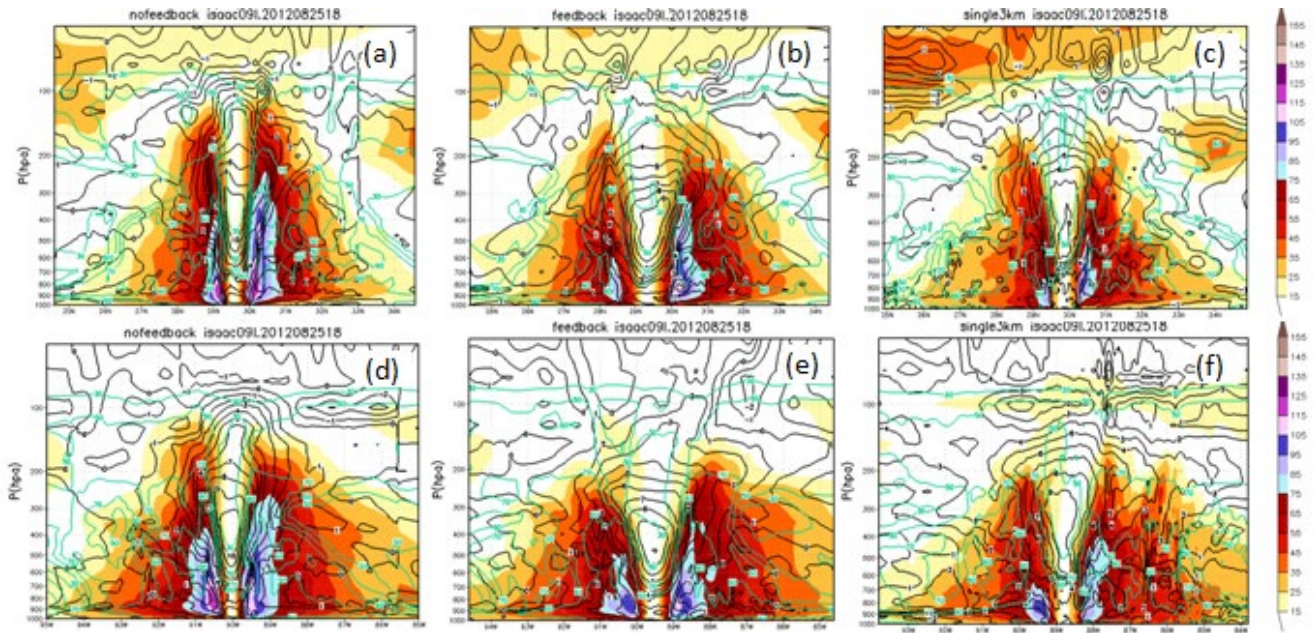


FIG. 3 North-South vertical cross-sections of wind speed (shaded), RH (green), and temperature perturbation (black) from runs of (a) one-way nesting, (b) two-way nesting, and (c) single 3-km at 72 hr. Same for (d), (e), and (f) except for West-East cross-sections.

4. Conclusions

Preliminary analyses suggest that the HWRf using moving nested grids with full two-way feedback can give comparable results to a single high-resolution domain run in terms of TC track, intensity, and structure. Many physics schemes are not yet fully scale/resolution-aware and, therefore, could account for the performance of runs using different resolutions. Improving the scale awareness of physics parameterizations is a priority for multi-scale high-resolution simulations. Given limited resources, especially in operations, a nesting technique is still a useful and effective way to simulate multi-scale weather events.